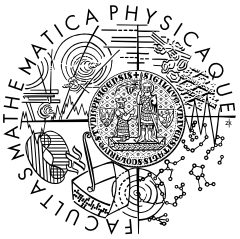

FACULTY
OF MATHEMATICS
AND PHYSICS
Charles University

Abstract of the doctoral thesis

Chromospheric waves and their contribution to heating of the atmosphere

Vahid Abbasvand Azar

Astronomical Institute of the Charles University, Faculty of Mathematics and Physics, Charles University

Astronomical Institute of the Czech Academy of Sciences, v.v.i.

Supervisor of the doctoral thesis: RNDr. Michal Sobotka, DSc.

Study programme: Theoretical Physics, Astronomy and Astrophysics

Study branch: P4F1

Prague 2021

The doctoral thesis was done at the Astronomical Institute of the Charles University, Faculty of Mathematics and Physics, Charles University and the training institution Astronomical Institute of the Czech Academy of Sciences, v.v.i., between 2017 and 2021.

PhD student: Mgr. Vahid Abbasvand Azar

Department: Astronomical Institute of the Charles University,
Faculty of Mathematics and Physics
V Holešovičkách 2
180 00 Praha 8
Czech Republic

Supervisor: RNDr. Michal Sobotka, DSc.
Astronomical Institute of the
Czech Academy of Sciences, v.v.i.
Fričova 298
251 65 Ondřejov
Czech Republic

Referees: ...
...
...
...
...

...
...
...
...
...

The defence of the thesis will be held on ... February 2022 at ... in front of the defence committee for the doctoral study branch P4F1 Theoretical Physics, Astronomy and Astrophysics at the address Ke Karlovu 3, Praha 2, in the room M252ZAS.

The thesis can be obtained in printed or electronic version through the Student Affairs Department of the Faculty of Mathematics and Physics of Charles University, Ke Karlovu 3, Praha 2.

Chairman of the programme P4F1: prof. RNDr. Pavel Krtouš, Ph.D.
Institute of Theoretical Physics MFF UK
V Holešovičkách 2
180 00 Praha 8
Czech Republic

Contents

Acknowledgements

I would like to offer my sincere gratitude to my supervisor Dr. M. Sobotka and my advisor Prof. P. Heinzel for their guidance and support throughout this thesis. I would also like to thank the solar physics team at the Leibniz-Institut für Astrophysik Potsdam (AIP), especially Dr. C. Denker, whose insight and knowledge into the subject matter steered me through this research.

During my doctoral studies I was supported by the Czech Science Foundation grant 18-08097J and by the project SOLARNET that has received funding from the European Union Horizon 2020 research and innovation programme under grant agreement No. 824135.

Abstract

Acoustic and magnetoacoustic waves play an important role in the chromospheric heating, exhibiting the capability of depositing a main part of their energy in the chromosphere. To study the heating of solar chromospheric magnetic and non-magnetic regions by acoustic and magnetoacoustic waves, the deposited acoustic-energy flux, derived from observations of strong chromospheric lines (Hα, Hβ, Ca II 854.2 nm, and Mg II k&h), is compared with the total integrated radiative losses. A set of quiet-Sun and weak-plage regions was observed with the Interface Region Imaging Spectrograph (IRIS), Vacuum Tower Telescope (VTT), Dunn Solar Telescope (DST) and Goode Solar Telescope (GST). The deposited acoustic-energy flux is derived from Doppler velocities observed at two different reference heights corresponding to the middle and upper chromosphere. A set of scaled non-LTE 1D hydrostatic semi-empirical models, obtained by fitting synthetic to observed line profiles, is applied to compute the radiative losses. In the quiet chromosphere, the deposited acoustic flux is sufficient to balance the radiative losses and maintain the semi-empirical temperatures in layers between the two reference heights. In the magnetic active-region chromosphere, the comparison shows that the contribution of magnetoacoustic energy flux to the radiative losses is only 10–30 %, so that the contribution is too small to balance the radiative losses in the chromosphere, which has to be heated by other mechanisms.

1 Introduction

The solar chromosphere is hotter than the photosphere and the increase of temperature in semi-empirical models of the chromosphere cannot be explained by radiative heating. There is no generally accepted picture of the energy transport processes responsible for this rise and a pure radiative transfer cannot explain the temperature given by semi-empirical models. Spectral lines typical for the chromosphere are strong hydrogen lines, Ca II K&H and infrared triplet, and the k&h lines of Mg II. Cores of these spectral lines are formed in conditions that are far from the local thermodynamical equilibrium (LTE). Radiative energy released in these lines from the quiet-Sun chromosphere is estimated to 4300 W m^{-2} excluding Lyman-α (Vernazza et al., 1981). In active regions, these losses are higher by a factor of 2–4 (Withbroe and Noyes, 1977). They have to be balanced by an energy input supplied by various heating mechanisms.

The scenarios of chromospheric heating processes can be divided into two main competitive categories (see Jess et al., 2015, for a review): (i) Reconnection of magnetic field lines with opposite directions leads to a conversion of magnetic to thermal energy (Testa et al., 2014). (ii) Propagation of waves in plasma: acoustic waves are generated by material motions in the upper convection zone and the energy of these waves is dissipated at some distance from the birth point due to the change of atmospheric properties along the vertical direction in a stratified medium (Zaqarashvili and Erdélyi, 2009; Kayshap et al., 2018). In this thesis, we focus to the latter mechanism.

The magnetic field acts as a catalyst in propagation of acoustic waves, without being destroyed in the process. Two different cases can be considered in quiet-Sun regions on account of the magnetic field topology: the more vertical field in solar magnetic network and the more inclined one in the intranetwork. Mostly vertical magnetic field lines in the photosphere can be more inclined in the chromosphere and expand in the atmospheric volume at some

height. This field expansion leads to canopy regions, which substantially reduce the energy flux carried by the waves (so-called magnetic shadows, Judge et al., 2001; Vecchio et al., 2007; Kontogiannis et al., 2010). On the other hand, inclined magnetic field reduces the magnetic cut-off frequency 5.2 mHz (Bel and Leroy, 1977; Cally, 2006), allowing the propagation of low-frequency waves into the chromosphere.

The physical properties of the solar chromosphere including its dynamics, energetics, and the formation of spectral-line features have been explored with significant efforts, using both theoretical simulations and observational analysis. Theoretical evidence shows that acoustic waves can heat the intranetwork (i.e., non-magnetic) regions on the Sun (Ulmschneider and Musielak, 2003). Based on simulations, Carlsson and Stein (1992) reported that when the acoustic wave dissipation is fully employed, the Ca II H line behavior is very similar to the observed one. Cuntz et al. (2007) discussed the physical nature of acoustic heating in the solar chromosphere using time-dependent 1D simulations to calculate wave energy fluxes. They claimed that high-frequency acoustic waves are sufficient to heat the intranetwork regions in the solar chromosphere.

A number of different solar atmospheric models derived from observations or theoretical simulations are used to study physical properties of solar atmosphere from the photosphere to the transition region. In the following, we will refer to the set of semi-empirical one-dimensional (1D) hydrostatic models, VAL A–F, presented by Vernazza et al. (1981), which describe the solar atmosphere from intranetwork to bright network features. In their theoretical review, Ulmschneider and Musielak (2003) claimed that acoustic waves can heat the intranetwork regions on the Sun. Many studies have been based on 3D heating simulations. Wedemeyer-Böhm et al. (2007) studied whether or not acoustic waves are sufficient to heat the quiet-Sun intranetwork regions. They compared TRACE observational data with a synthetic image obtained from a 3D simulation and demonstrated that these observations of intranetwork regions can be reproduced without a strong need for magnetic fields. In a similar work, Cuntz et al. (2007) also showed that high-frequency acoustic waves can heat those regions in the solar chromosphere. Some recent works have shown that heating by waves partly balances the radiative losses of the chromospheric layers (Jefferies et al., 2006; Kalkofen, 2007; Bello González et al., 2010; Kanoh et al., 2016; Grant et al., 2018; Abbasvand et al., 2020a,b), while some other studies have declared that the total acoustic flux energy is still insufficient to heat the quiet-Sun regions (Fossum and Carlsson, 2005; Carlsson et al., 2007; Beck et al., 2009).

The dissipation of acoustic waves is a multi-dimensional time-dependent process and difficulties come from the modeling and its high computational requirements, which do not allow us to represent the observed chromospheric structures directly this way (Carlsson and Leenaarts, 2012). A review on radiation-hydrodynamic models of the solar atmosphere was recently published by Leenaarts (2020).

In an alternative stationary approach, time averaged atmospheric parameters of 1D semi-empirical hydrostatic models were used to show that acoustic energy flux deposited in the chromosphere provides a remarkable source of energy required to balance the local radiative losses (Sobotka et al., 2016).

Our present work continues in this approach. Recently, we (Abbasvand et al., 2020a) introduced a new grid of 1D semi-empirical hydrostatic models by scaling the temperature and column mass of six initial VAL A–F models by Vernazza et al. (1981) to refine the comparison of the deposited acoustic flux with radiative losses. Further, (Abbasvand et al., 2020a,b) we analyzed four observations of quiet-Sun and weak active regions in the lines Ca II 8542 Å, Hα, and Hβ. We demonstrated that the radiative losses can be fully balanced by the deposited

acoustic energy flux in the middle chromosphere of a quiet Sun region, which was far enough from any extended canopy region. The acoustic energy flux was reduced by a factor of 2–3 in the quiet-Sun region that was close to a plage and a pore. In the upper chromosphere, the contribution of the deposited acoustic flux energy to the released radiative energy was small, less than 20% both in quiet and active regions. No clear conclusion was obtained for the middle chromosphere of active regions due to a lack of data. Finally we (Abbasvand et al., 2021) studied the heating of the solar chromosphere by dissipation of (magneto)acoustic waves in the middle and upper chromosphere using IRIS spectroscopic observations in the Mg II k&h lines. We have shown that the deposited acoustic flux can fully balance the energy released by radiation in quiet-Sun regions between the heights 900 and 2200 km. A dissipation of supersonic shocks can be a major contributor to the radiative losses.

2 Observations

We examined the heating of the solar chromosphere by dissipation of (magneto)acoustic waves through different layers of the solar chromosphere using data from the Interferometric Bidimensional Spectrometer (IBIS, one data set) at the Dunn Solar Telescope (DST), the echelle spectrograph attached to the Vacuum Tower Telescope (VTT, two data sets), the Fast-Imaging Solar Spectrograph (FISS) attached to Goode Solar Telescope (GST) at the Big Bear Solar Observatory (BBSO, one data set), and the space-born Interface Region Imaging Spectrograph (IRIS, 23 data sets). The combination of these instruments provided multi-line observations in Hα, Hβ, Ca II 854.2 nm and Mg II k and h (2796.35 Å and 2803.52 Å, respectively) lines. The targets were quiet-Sun and weak active regions located close to the center of the solar disc, to minimize possible projection effects (Ghosh et al., 2019). The raw data were calibrated using standard dark- and flat-field procedures.

The Doppler velocities were measured for two purposes: (1) to remove Doppler shifts from the spectroscopic observations to calculate time-averaged line profiles and (2) to obtain purely chromospheric Doppler velocities required for the calculation of acoustic fluxes (see Section 3.2). In the VTT and GST data sets, we applied a bisector routine that returns line shifts at pre-selected intensity levels in the line profile and the shift of the line centre was derived from a parabolic fit around the minimum intensity. In the IBIS data set we used the double-slit method (Garcia et al., 2010), which provided Doppler shifts of the inner wings of the Ca II 854.2 nm line, and the parabolic fit of the line center. The whole line profiles were then moved back to zero-shift positions and the time-averaged line profiles were calculated.

To obtain the chromospheric velocities, we used the line-center shifts of Hα and Ca II 854.2 nm lines and bisector shifts of Hβ and Ca II at line-profile intensity levels corresponding respectively to wavelength distances of $\pm$18 pm and $\pm$13 pm from the line center, which were found from contribution functions (see Section 3.1). The shifts were converted into the Doppler velocities assuming that the quiet-Sun regions within the field of view are at rest on average.

In IRIS data sets, Doppler shifts of the emission core, including both emission peaks, were measured by means of the improved double-slit method (Abbasvand et al., 2021). We selected the "slit" distance to match the half intensity difference between the emission maximum and the absorption-profile minimum, so that shifts of the whole emission core were measured independently of the emission peaks and central reversal. Because the widths of the k&h emission cores change with physical conditions in the chromosphere, the "slit" distance was adapted to the emission-core width measured for each time instant and position along the

spectrograph slit. We looked for the positions of the central reversal and the emission core in a spectral region 2.05 Å (40 pixels) wide around the approximate line center. The central-reversal position was determined by means of the 3-point parabolic fit of the profile minimum between the two emission peaks. For those profiles where the central reversal was missing (single-peaked emission profiles), the central-reversal velocity was set to zero and marked as an outlier.

3 The method

The applied method calculates the acoustic energy flux deposited in a chromospheric layer between two reference geometrical heights and compares it with radiative losses computed from model atmospheres and integrated over the same height range. The reference heights are determined with regard to typical formation heights of the observed spectral lines.

3.1 Model atmospheres

The initial semi-empirical models VAL A–F include the column mass m, optical depth τ_{500} at 500 nm, temperature T, microturbulent velocity $v_{\rm t}$, hydrogen density $n_{\rm H}$, electron density $n_{\rm e}$, total pressure $P_{\rm tot}$, gas pressure $P_{\rm g}$, and density ρ as a function of geometrical height h. To approximate the physical conditions in the ROIs, these initial models are scaled by changing two free parameters $p_{\rm T}$ and $p_{\rm m}$ that define the T and m stratifications (see Abbasvand et al., 2020a, for details). Figure 1 shows an example how all the VAL models can be reproduced by scaling of the VAL C model.

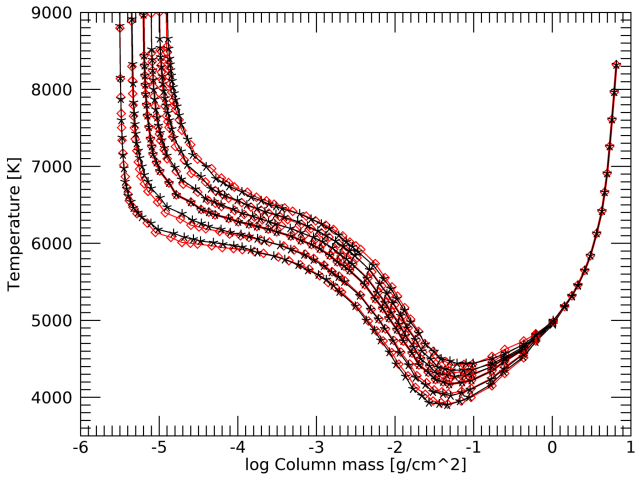

Figure 1: Temperature versus column mass plots of the VAL A-F models scaled from the model C. Red and black lines show the scaling results and the original VAL models, respectively. The symbols denote sampling of the models.

These stratifications are used as inputs in the non-LTE radiative-transfer code based on the Multi-level Accelerated Lambda Iterations technique (MALI, Rybicki and Hummer, 1991, 1992) with standard partial frequency redistribution (PRD). The hydrogen version of the code (with PRD in Lyman lines) computes the ionization structure and populations of hydrogen levels using a 5-level plus continuum atomic model. It re-computes the complete scaled atmospheric models and calculates synthetic profiles of the Hα and Hβ lines. Then, the Ca II and Mg II versions of the code (with PRD in the K and H lines of Ca II and k and h lines

of Mg II) are run to to calculate synthetic profiles of the Ca II 854.2 nm line and the Mg II k&h lines, the net radiative cooling rates, and contribution functions for each height in the model. For each of the initial VAL models, a grid of 2806 scaled models is computed using a combination of 61 and 46 possible values of $p_{\rm T}$ and $p_{\rm m}$, respectively. In total, a grid of 16836 models, parameterized by the initial model selection, $p_{\rm T}$, and $p_{\rm m}$, is available (Abbasvand et al., 2020a). This grid describes the solar atmosphere from dark intranetwork areas to bright network features.

The initial models are assigned to different areas in region of interests (ROIs) in accordance with the line-core intensity of the observed chromospheric lines. Then, a scaled model from the grid, which provides the best match of the synthetic to the local time-averaged observed profiles, is selected at each position within the ROIs. The best match means that the sum of squared differences between the synthetic and observed profiles of all lines under study (merit function) is at minimum.

Physical quantities, which are used to calculate acoustic fluxes (see Section 3.2), are retrieved from the models at reference heights that are common for all models in a ROI. These heights also delimit integration ranges of radiative losses. The reference heights are selected with regard to formation heights of the observed spectral lines, properly speaking, formation heights of parts of line profiles utilized to measure Doppler velocities. The formation heights can be obtained from a contribution function $C_\nu(h)$, which describes the contribution of different atmospheric layers to the emergent intensity of radiation I_ν at the considered frequency ν (e.g., Gurtovenko et al., 1974),

$$I_\nu = \int C_\nu(h)\,{\rm d}h. \tag{1}$$

In quiet- and active-Sun atmospheric models, $C_\nu(h)$ of Hα, Hβ, Ca II 854.2 nm and Mg II k and h lines are computed by the non-LTE radiative-transfer codes described above. Contribution functions computed from two typical models that characterize the quiet Sun (BBSO data set) and bright chromospheric features (VTT data sets) are plotted for different wavelength distances $\Delta\lambda$ from the line center and different heights h in Figure 2. We can see that the central parts of line profiles are formed largely in the chromosphere, each of them in different ranges of heights.

The typical formation height can be calculated as a mean h weighted by $C_\nu(h)$ at a given $\Delta\lambda$. We obtained typical formation heights using all models in each ROI and found the most frequent ones. The Hα line center is formed typically at 1800 km in the quiet-Sun atmosphere and at 1900 km in bright chromospheric features. For the Ca II 854.2 nm line in the quiet Sun, the typical formation height of the line center is 1400 km and the inner wings at $\Delta\lambda = \pm 13$ pm are formed at 1000 km. The selection of $\Delta\lambda$ for Hβ and Ca II was intended to reach the deepest possible chromospheric layers with a minimum contribution from the photosphere. The most frequent typical formation heights, stated above, were accepted as the reference heights for the calculation of radiative losses and deposited acoustic fluxes.

In the IRIS data sets, we found effective formation heights of those parts of the line profile where the Doppler velocities are measured, that is, the central reversal ($h_2, \Delta\lambda = 0$) and the half-maximum intensity of the emission core (h_1). Here, $\Delta\lambda$ varies in the range 0.20–0.23 Å for the k line and 0.18–0.21 Å for the h line, according to the model atmosphere. We obtained effective formation heights h_1 and h_2 for all models assigned along the slit of each IRIS data set. The Mg II k and h lines behave similarly. The emission core of the k line is formed only by a few tens of kilometers higher then the core of the h line, so that we define the effective

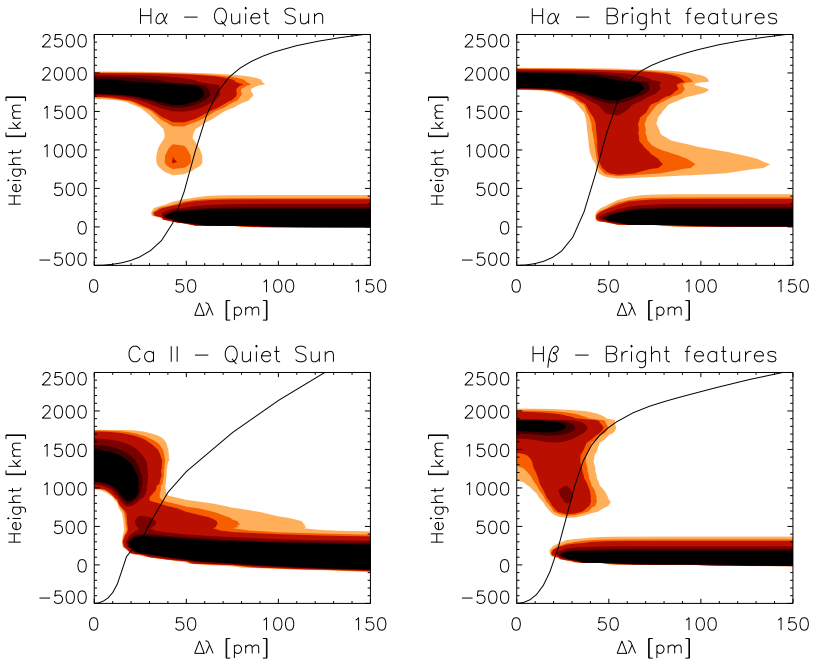

Figure 2: Contribution functions of the Hα, Hβ, and Ca II 854.2 nm lines for two typical models derived from our observations – quiet Sun (*left*) and bright chromospheric features (*right*). The colors change from light orange to black with increasing values of the contribution function. Black lines show corresponding synthetic line profiles.

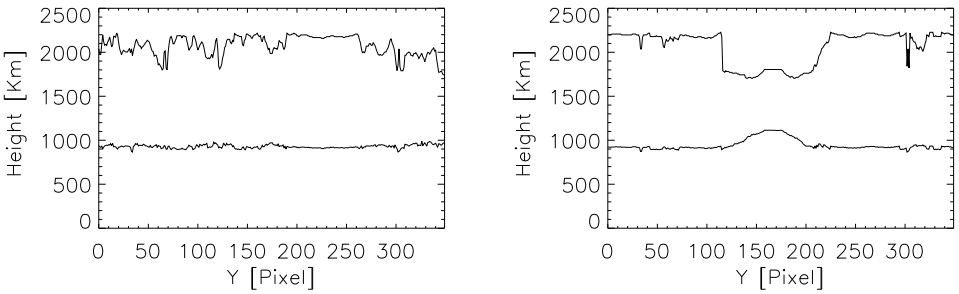

Figure 3: Lower and upper effective formation heights of the Mg II lines in the typical quiet-Sun IRIS data set (left) and active-region data set (right) are plotted versus the position along the spectrograph slit.

formation heights h_1 and h_2 as the average of heights obtained for both lines and adopt them for the reference ones.

Figure 3 shows these heights in typical quiet- and active-Sun data sets. We see that the effective formation heights of the central reversal at most of the positions in the quiet Sun, characterized by low-temperature model atmospheres, are between 2000–2200 km, while those of active regions (hot models) are mainly in the range of 1700–1900 km. For the emission core, the effective formation heights are in the range 900–1000 km and 1000–1200 km in quiet and active regions, respectively.

The net radiative cooling rates (radiative losses) characterize the energy released by radiation from the chromosphere. These also indicate the amount of non-radiative heating that maintains the semi-empirical temperature at a given height in the solar atmosphere. To calculate them, we use the scaled models assigned to each pixel in a ROI. For each model,

they are computed for the main contributors in the solar chromosphere, namely, the lines Ca II H & K, the Ca II infrared triplet, Mg II h & k, hydrogen Lyman and Balmer lines, and hydrogen continua, using our non-LTE radiative transfer codes MALI. The total net radiative cooling rates, a sum of the main contributors, are integrated over the geometrical height in the range between the reference heights for each pixel in the ROIs.

3.2 Deposited acoustic flux

Velocity oscillations at each position in the ROIs are studied using standard Fourier analysis of the time series of Doppler maps measured in the line centers of Hα and Ca II 854.2 nm and at $\Delta\lambda = \pm 18$ pm and $\Delta\lambda = \pm 13$ pm from the line centers of Hβ and Ca II 854.2 nm, respectively. In the IRIS data sets, the Doppler velocities were measured in the central reversals and at the half-maximum intensity of the emission cores of the Mg II k&h lines. The maximum detectable frequencies of velocity oscillations were in the range of 9.6–24 mHz which is sufficient to investigate the power spectra in the quiet-Sun and magnetic regions in the chromosphere. The method of power-spectra calculation and calibration in absolute units is described by Rieutord et al. (2010).

The acoustic-energy flux at a given height in the chromosphere is estimated following the method of Bello González et al. (2009), assuming that (i) the acoustic waves propagate upwards and (ii) the inclination of magnetic field along the track of acoustic waves is equal to that measured in the photosphere. It can be formulated as

$$F_{\rm ac}(\nu) = \rho\, P_v(\nu)\, v_{\rm gr}(\nu)/TF(\nu), \tag{2}$$

where ρ is the gas density at the given height, P_v the spectral-power density derived from the Doppler velocities, and $TF(\nu)$ is a transfer function of the atmosphere. The transfer function relates to the transmission of the wave amplitudes by the solar atmosphere as a function of frequency. It is proportional to the ratio of the velocity amplitude observable as a Doppler shift of the given line to the true amplitude. Its value is unity if the entire wave signal is observed as the Doppler shift of the spectral line throughout the atmosphere at a given frequency, whereas values smaller than unity represent some loss of the signal because of the extent in height of the spectral-line contribution functions. In general, the most affected are short-period (small-scale) fluctuations. A detailed time-dependent model of the atmosphere is needed to derive this value. We set this function equal to unity for all frequencies, which means that the observed Doppler signal of all waves at a given frequency is detected throughout the solar atmosphere (Sobotka et al., 2016). This rough approximation may lead to underestimated acoustic-flux values at higher frequencies.

The group velocity for vertical energy transportation $v_{\rm gr}$ is given by

$$v_{\rm gr} = c_{\rm s}\sqrt{1-(\nu_{\rm ac}/\nu)^2}, \tag{3}$$

where $\nu_{\rm ac} = \gamma g \cos\theta/(4\pi c_{\rm s})$ is the acoustic cut-off frequency and $c_{\rm s} = \sqrt{\gamma P_{\rm g}/\rho}$ the sound speed. Here, γ is the adiabatic index equal to 5/3 for monoatomic gas, g the surface gravity, and θ the magnetic-field inclination in the photosphere, which reduces the acoustic cut-off frequency (Cally, 2006). For $\nu_{\rm ac}$ we adopt the value $5.2\cos\theta$ mHz. The total acoustic flux at all frequencies between $\nu_{\rm ac}$ and the maximum detectable frequency $\nu_{\rm max}$ is

$$F_{\rm ac,tot} = \int_{\nu_{\rm ac}}^{\nu_{\rm max}} F_{\rm ac}\, {\rm d}\nu. \tag{4}$$

The values of gas pressure P_g and density ρ are taken in each pixel of the ROIs from the corresponding scaled model atmosphere at two reference heights h_1 and h_2. The deposited acoustic flux ΔF_{ac} is the difference between the incoming acoustic energy flux at the lower reference height h_1 and the outgoing one at the upper reference height h_2,

$$\Delta F_{ac} = F_{ac,tot}(h_1) - F_{ac,tot}(h_2). \quad (5)$$

A part of the incoming energy flux is dissipated in the chromosphere between h_1 and h_2 and likely converted into radiation, while the outgoing part continues to propagate higher in the atmosphere.

4 Results

A quantitative comparison of deposited acoustic energy flux with total integrated radiative losses is done. The comparisons are made in the middle and upper chromosphere of the quiet Sun and weak plage regions located in the central zone of solar disc. The spectral lines Hα, Hβ, Ca II 854.2 nm and Mg II k&h provide information about different ranges of heights in the chromosphere according to their effective formation heights in quiet and active areas. For the middle chromosphere, two different ranges are used, 900–1500 km in the IBIS data set and 1000–1400 km in the BBSO data set. At a short notice, in IBIS ROI the models are derived from VAL B, where the formation heights are lower compared to VAL C, which is used in BBSO ROI. In the same manner, in the upper chromosphere the ranges are set to 1400–1800 km in BBSO and 1600–1900 km in VTT data sets. In the IRIS data, the height ranges vary from 900–2100 km in quiet regions to 1100–1900 km in active ones. The deposited acoustic fluxes ΔF_{ac} and the total radiative losses L are computed for those height ranges.

In the IBIS data set, we calculate the deposited acoustic fluxes using two different sets of magnetic-field inclinations to estimate the influence of uncertainties in the inclination angle: (1) original inclination angles retrieved from the inversion, including the unreliable values near 90° in weak-field or nonmagnetic regions. (2) Corrected inclination angles, where the unreliable values are set to zero where the magnetic-field strength was lower than 125 G. Scatter plots of total integrated radiative losses L versus the acoustic energy flux ΔF_{ac} deposited in the chromosphere between h=900–1500 km are shown in Figure 4(a) and (b) for the original inclination angles and the corrected ones, respectively. The red solid line represents mean values of ΔF_{ac} that fall into 200 W m^{-2} wide bins of the L histogram. The bins must contain at least 100 points to calculate the mean value. Likewise, the green line represents median values. The red dashed lines delimit the $\pm 1\sigma$ range that characterizes the scatter of individual points in each bin. When the unreliable horizontal magnetic inclination is included (Figure 4(a)), the deposited acoustic fluxes in the quiet-Sun area (L$<$ 5000 W m^{-2}) almost double those calculated using the corrected inclination values (Figure 4(b)). This is not realistic because of too many points where $\Delta F_{ac} > L$. The increase of ΔF_{ac} is much smaller in the plage, where the magnetic inclination is determined reliably. We used the deposited acoustic fluxes calculated using the corrected inclination angles.

It appears that the deposited acoustic-flux energy in the middle chromosphere of quiet Sun balances 30 %–50 % of the energy released by radiative losses. The energy carried by (magneto)acoustic waves in the plage supplies 50 %–60 % of the radiated energy at locations with a vertical magnetic field and 70 %–90 % in regions where the magnetic field is inclined more than 50°. These values are statistical averages of results with a large individual scatter.

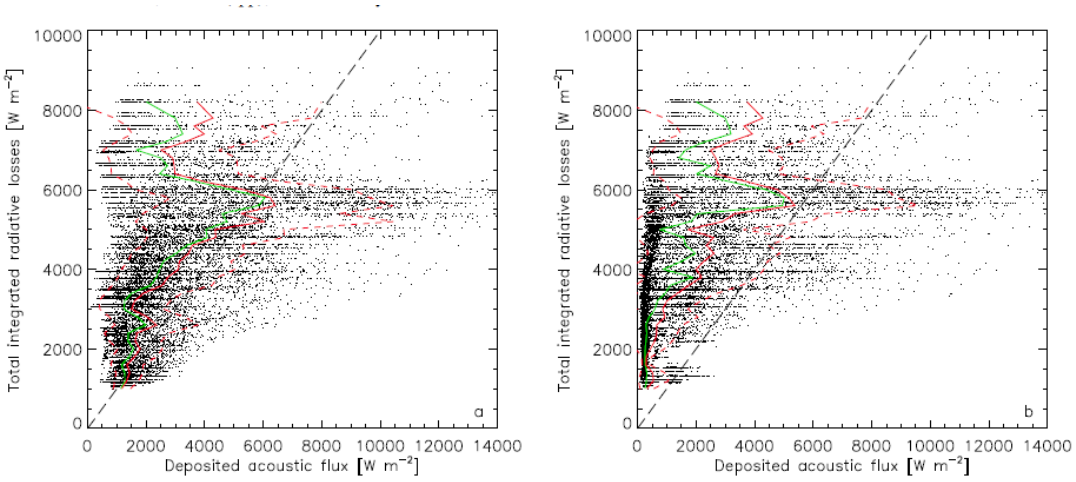

Figure 4: Scatter plots of total integrated radiative losses vs. deposited acoustic flux in the IBIS ROI. The acoustic fluxes are calculated using (*a*) the original magnetic inclination angles and (*b*) the corrected ones. Solid lines show average (red) and median (green) values together with red dashed lines of $\pm 1\sigma$. The straight dashed line represents the full balance of radiative losses by acoustic-flux deposit.

We also have to note that the area considered as quiet Sun in the IBIS ROI is close to the plage and it falls within the extended canopy region of the plage's magnetic field. The effect of "magnetic shadows", which are related to the elevated magnetic field forming the Ca II fibrils (Vecchio et al., 2007; Kontogiannis et al., 2010), reduces the oscillatory power in this region. Consequently, the deposited acoustic flux in this quiet-Sun area may be lower than that in quiet regions far from the plage. Compared to the results of Sobotka et al. (2016), the median values of $\Delta F_{\rm ac}$ are consistent except the brightest parts of the plage ($L > 6500$ W m^{-2}), where the magnetic inclination was overestimated. Moreover, the revision of the magnetic inclination map resulted in an increase of $\Delta F_{\rm ac}$ at the plage periphery ($L \simeq 6500$ W m^{-2}). Other differences can be explained by improved values of the gas density, to which the acoustic fluxes are directly proportional. The present set of 1737 atmospheric models provides a more realistic density distribution than the simple grid of only seven models.

In the two VTT data sets, the deposited acoustic fluxes $\Delta F_{\rm ac}$ and total integrated radiative losses L are computed and integrated for the range $h = 1600$–1900 km in the upper chromosphere. The maps of $\Delta F_{\rm ac}$ and L for both ROIs are displayed in Figure 5. Enhanced radiative losses of the order 10^4 W m^{-2} are observed in the central part of the plage on June 6, 2019. This area is characterized by hot atmospheric models, obtained by scaling the initial model VAL F, for which a strong contribution of hydrogen Lyman-α to L at $h > 1800$ km becomes important.

Figure 6 shows the scatter and density plots comparing $\Delta F_{\rm ac}$ and L for both ROIs. For all plotted points, the deposited acoustic flux is mostly in the range from -50 W m^{-2} to 150 W m^{-2} and it is very small compared to the radiative losses. Its mean values are approximately 30 W m^{-2} for the 2018 December 11 data set and zero for the 2019 June 6 one. The small positive mean value of the December flux is a consequence of the high-frequency contribution induced probably by the seeing. In the density plots (Figure 6 *right*), pixels of magnetic and non-magnetic areas are separated and their densities are normalized to the common histogram

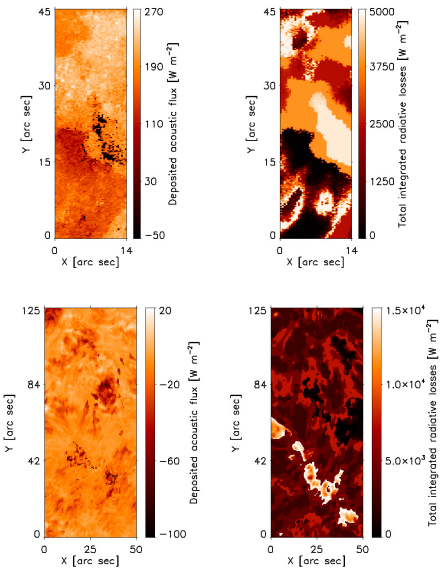

Figure 5: The deposited acoustic energy flux (*left*) and the total integrated radiative losses (*right*) for the range h=1600–1900 km (upper chromosphere) in the VTT ROIs of 2018 December 11 (*top*) and 2019 June 6 (*bottom*).

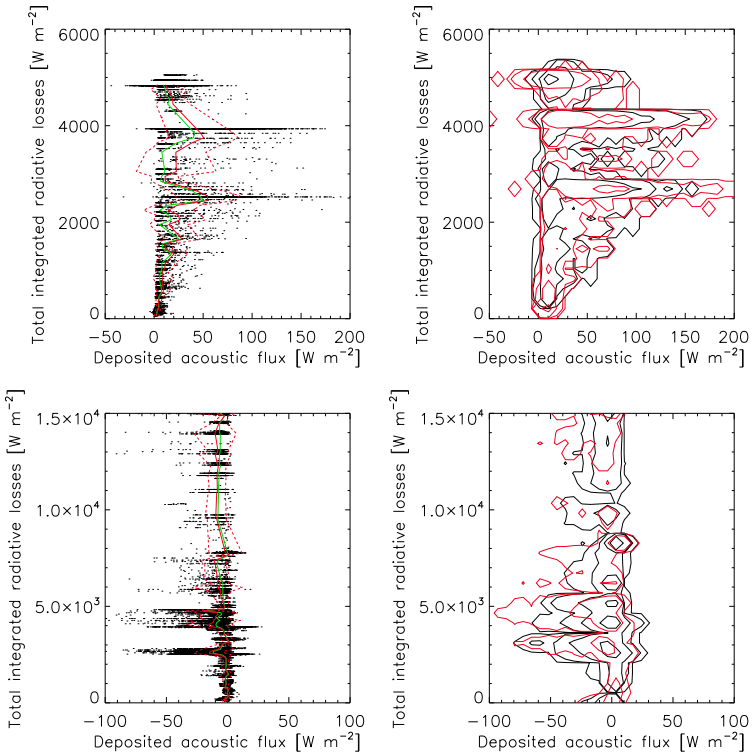

Figure 6: *Left*: Scatter plots of total integrated radiative losses versus deposited acoustic flux for the range h=1600–1900 km in the VTT ROIs of December 2018 (*top*) and June 2019 (*bottom*). Solid lines show average (red) and median (green) values together with red dashed lines of $\pm 1\sigma$. *Right*: Density contours of the scatter plots. Contours for magnetic (red) and non-magnetic (black) areas are plotted separately at density levels of 0.03, 0.3, 3, and 30 % of a common density maximum.

maximum of the two areas. The bin size of the 2D histogram is 30 W m^{-2} × 30 W m^{-2}. Contours are plotted at four density levels with a step of one order of magnitude, beginning at 0.03 % of the maximum. The magnetic areas of the December and June data sets include 33.0 % and 3.9 % of pixels in the ROIs, respectively.

Analogous scatter and density plots are shown in Figure 7 for the BBSO data set. The total radiative losses integrated over the 400 km thick layer in the middle chromosphere are $1000 < L < 2600$ W m^{-2} in the quiet area and reach 4300 W m^{-2} in two small bright

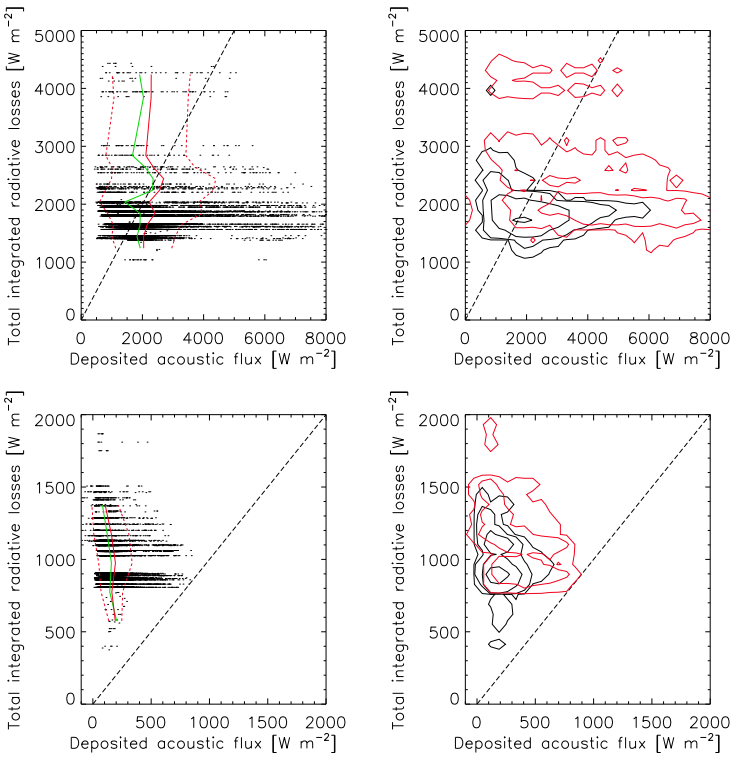

Figure 7: *Left*: Scatter plots of total integrated radiative losses versus deposited acoustic flux in the ROI of the BBSO data set. *Top*: $h = 1000$–1400 km, *bottom*: $h = 1400$–1800 km. Solid lines show average (red) and median (green) values together with red dashed lines of $\pm 1\sigma$. *Right*: Density contours of the scatter plots. Contours for magnetic (red) and non-magnetic (black) areas are plotted separately at density levels of 0.03, 0.3, 3, and 30 % of a common density maximum. Straight dashed lines represent the full balance of radiative losses by acoustic-flux deposit.

points connected with magnetic elements. The ratio of the mean deposited acoustic flux to the radiative losses $\overline{\Delta F_{\rm ac}}/L$ is between 0.9 and 1.3 in the quiet area, so that the acoustic energy flux balances the energy released by radiation (top panels in Figure 7). However, the contribution of $\overline{\Delta F_{\rm ac}}$ to L in the two bright points is only 60 %. In the upper chromosphere at the heights 1400–1800 km, the radiative losses ($400 < L < 1900$ W m^{-2}) are larger than the deposited acoustic flux for all the points in the scatter plot (bottom panels in Figure 7) and $\overline{\Delta F_{\rm ac}}/L \simeq 0.2$. This means that the deposited acoustic flux is insufficient to balance the radiative losses and maintain the semi-empirical temperature at these heights. Negative values of $\Delta F_{\rm ac}$ appearing at some scarce locations in the ROI are caused by the limited accuracy of our method.

In the IRIS observations, 23 different data sets including 12 quiet-Sun and 11 active regions are utilized to compare $\Delta F_{\rm ac}$ and L in the middle and upper chromosphere. The quiet-Sun atmospheres were represented by scaled initial VAL C and D models, providing the best match of synthetic to local-time averaged observed profiles. In the case of active-region atmospheres, best-matching models from the grids of scaled initial VAL E and F models were selected.

Relations between the acoustic fluxes and total integrated radiative losses are shown for two data sets typical for the quiet Sun and active region in Figure 8. The first row in the figure displays the effective formation heights. The second row shows the incoming acoustic fluxes $F_{\rm ac}(h_1)$ (black line) and the outgoing ones $F_{\rm ac}(h_2)$ (multiplied by ten, blue line) for each position along the slit. A fraction of the incoming energy flux is dissipated in the chromosphere between h_1 and h_2 and the rest continues to propagate higher in the atmosphere. The deposited acoustic energy fluxes $\Delta F_{\rm ac}$ (red) and the total integrated radiative losses L (black) are compared in the third row. Finally, scatter plots of L versus $\Delta F_{\rm ac}$ are displayed in the fourth row.

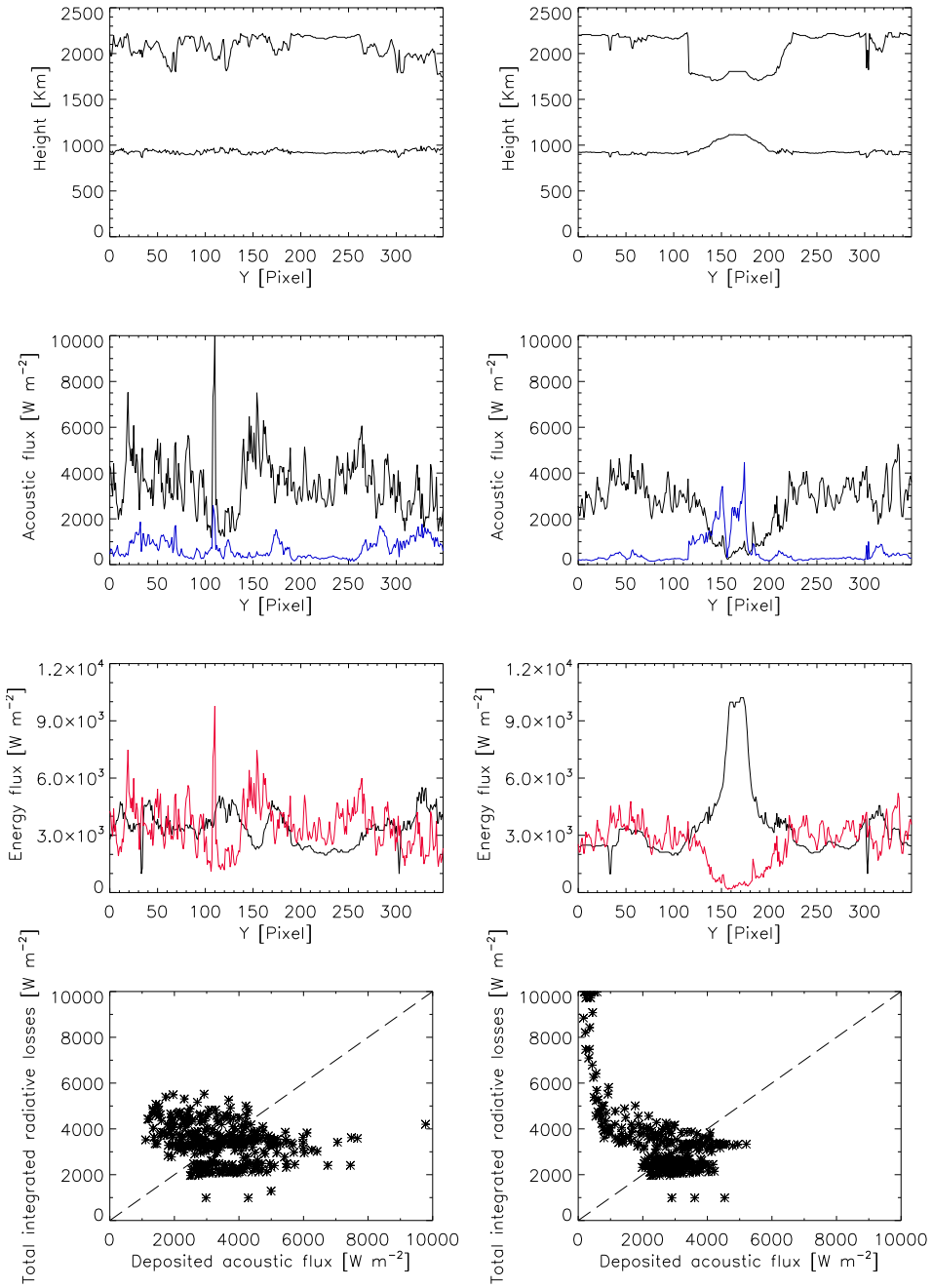

Figure 8: IRIS: lower and upper effective formation heights (*first row*), acoustic fluxes (*second row*), and energy fluxes (*third row*) along the slit in the typical quiet-Sun data set (*left*) and active-region data set (*right*). In the acoustic-flux plots, black lines correspond to incoming acoustic fluxes and blue ones to outgoing acoustic fluxes multiplied by 10. In the energy-flux plots, red lines correspond to deposited acoustic fluxes and black ones to total integrated radiative losses. Scatter plots of these quantities are in the *fourth row*. Straight dashed lines represent the full balance of radiative losses by acoustic-flux deposit.

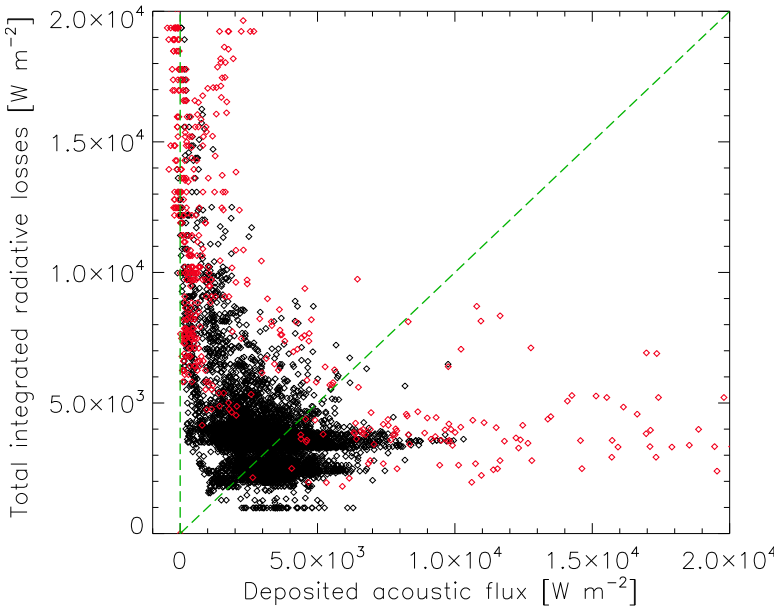

Figure 9: Scatter plot of total integrated radiative losses versus deposited acoustic flux in all 23 IRIS data sets. Black and red diamonds correspond to non-magnetic and magnetic positions, respectively. Straight dashed lines represent the full balance of radiative losses by acoustic-flux deposit and zero deposited acoustic flux.

Figure 9 illustrates the scatter-plot comparison of $\Delta F_{\rm ac}$ and L for all positions along the slits in all 23 IRIS data sets. Points located in non-magnetic regions (6337 in total) are distinguished from those (524) of magnetic regions with $|B| > 125$ G. All the observed quiet and active regions behave similarly to the example shown in Figure 8. In quiet-Sun regions ($L < 5000$ W m^{-2}), $\Delta F_{\rm ac}$ is statistically comparable to L, meaning that the energy released by radiation can be balanced by the deposited acoustic flux. In active regions ($L > 5000$ W m^{-2}), $\Delta F_{\rm ac}$ supplies only 10–30% of the radiated energy and even 5% for $L > 10000$ W m^{-2}. This is caused mainly by the observed reduction of incoming acoustic flux in active regions, which is probably due to the magnetic-canopy effect. Another reason is that 10–20% of the incoming acoustic flux is not deposited in the layer under study.

We also studied properties of observed waves using wavelet analysis of the IRIS Dopplergrams at the lower and upper boundaries. The wavelet coherence spectra provided phase shifts between the two boundaries. The average phase shifts for the non-magnetic and magnetic regions are positive (Fig. 10), so that the direction of propagation of the (magneto)acoustic waves is upward through the solar chromosphere. The phase speeds of the signals with frequencies larger than 2 mHz are supersonic. The increase of phase speed with frequency in non-magnetic regions is consistent with the presence of supersonic shocks. In magnetic regions, the phase speed is roughly constant in the frequency range 3–5 mHz, which is an indication of supersonic magnetoacoustic fast modes.

5 Conclusions

We examined the heating of the solar chromosphere by dissipation of (magneto)acoustic waves through different layers of the solar chromosphere using the DST/IBIS, VTT/echelle spectrograph, GST/FISS (BBSO), and IRIS spectroscopic multi-line observations in Hα, Hβ, Ca II 854.2 nm and Mg II k&h lines. The deposited acoustic energy fluxes were quantitatively

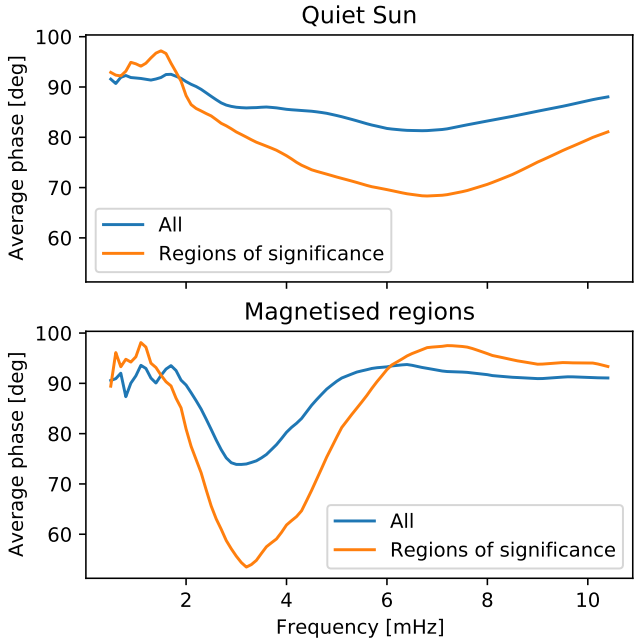

Figure 10: Average wave phase shifts between the upper- and lower-height boundaries of the IRIS chromospheric layer under study plotted separately for the non-magnetic (upper panel) and magnetic (lower panel) pixels. The averages are plotted for all contributions in the time-frequency wavelet spectrum (blue) and only for those contributions, where a statistically significant wavelet coherence was indicated (orange).

compared with the total radiative losses in quiet-Sun and weak active regions in the central zone of the solar disc.

The deposited acoustic flux was derived from time series of Dopplergrams measured in the centers and wings of strong chromospheric lines. We made use of 1D non-LTE hydrostatic semi-empirical models to calculate the radiative losses L, which were assigned to each pixel of each data set together with the deposited acoustic fluxes $\Delta F_{\rm ac}$. The models were selected from a grid obtained by scaling the temperature and column-mass stratifications of the initial VAL models to provide the best match of the synthetic to the observed time-averaged profiles. We compared L and $\Delta F_{\rm ac}$ in the chromospheric layer delimited by the upper and lower boundaries.

The IBIS data set provided information about the middle chromosphere between fixed reference heights 900 and 1500 km. The Doppler velocities were measured in the inner wings and center of the line Ca II 854.2 nm and the maximum detectable frequency of oscillations was 9.6 mHz. The average ratio $\Delta F_{\rm ac}/L$ was 0.3–0.5 in quiet and 0.5–0.7 in active regions. The upper chromosphere between the reference heights of 1600 and 1900 km was studied using the VTT observations in the Hβ line wings and Hα center, with the maximum detectable frequency of 20 mHz. The average ratio $\Delta F_{\rm ac}/L$ was practically zero in quiet as well as active regions.

The BBSO (FISS) quiet-Sun data set included the lines Ca II 854.2 nm and Hα, so that it was possible to measure Doppler velocities at three reference heights, distinguishing between the middle and upper chromosphere. The reference heights were at 1000, 1400, and 1800 km, corresponding to Ca II wings, Ca II center, and Hα center, respectively. The maximum detectable frequency was 20 mHz. The average ratio $\Delta F_{\rm ac}/L$ was 0.9–1.3 in the middle and 0.2 in the upper chromosphere.

In the IRIS data sets, the Doppler velocities were measured in the central reversals and at the half-maximum intensity of the emission cores of the Mg II k&h lines. On average, the central reversals were formed at the heights of 2200 km in quiet regions and 1800 km in

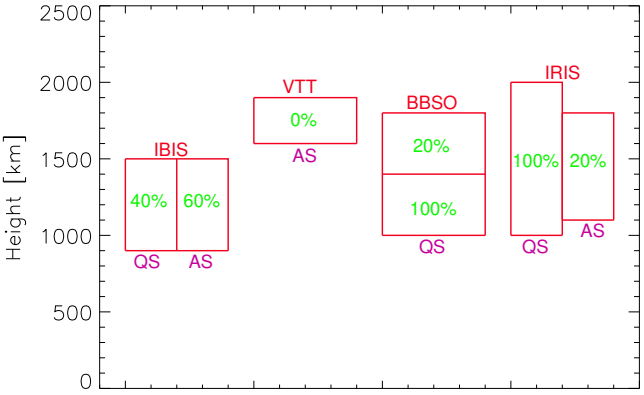

Figure 11: Average contributions of the deposited acoustic fluxes to radiative losses in quiet-Sun (QS) and active-Sun (AS) regions in different data sets used in this study.

active regions, setting the upper boundary of the studied chromospheric layer. The lower boundary was defined by the average formation height of the emission cores, 900 km in quiet regions and 1100 km in active regions. The lower and upper boundaries delimited a broad layer that included the middle together with the upper chromosphere. Individual heights of these boundaries varied with the model atmosphere. The maximum detectable frequencies of velocity oscillations were in the range of 14–24 mHz. The average ratio $\Delta F_{\rm ac}/L$ was 0.9–1.5 in quiet and 0.1–0.3 in active regions.

Figure 11 shows the results of comparison of the deposited acoustic fluxes with radiative losses in different layers of the chromosphere in quiet-Sun (QS) and active-Sun (AS) regions of all data sets together with their average contributions $\Delta F_{\rm ac}/L$.

We have shown that the deposited acoustic flux can fully balance the radiative losses in the layers between 900 and 2200 km in *quiet-Sun regions* of the IRIS observations. A dissipation of supersonic shocks can be a major contributor to the radiative losses (Abbasvand et al., 2021). This result is in agreement with the results obtained from the BBSO and VTT data sets showing that the acoustic flux deposited in the middle chromosphere (1000–1400 km) of a quiet region balanced completely the radiative losses and that its contribution in the upper chromosphere above 1400 km was very small (Abbasvand et al., 2020b).

We have to remark that these quiet-Sun regions were far from plages and their canopies formed by extended magnetic-field lines. Otherwise, the acoustic energy flux can be reduced by a factor of 2–3 in quiet regions that are close to plages or pores (IBIS data set, Abbasvand et al., 2020a) due to the presence of magnetic shadows (Vecchio et al., 2007; Kontogiannis et al., 2010). Thus, the effect of magnetic shadows, related to the elevated magnetic field of the canopy, reduced the oscillatory power and the deposited acoustic flux. The quiet-Sun region studied in the BBSO data set was far from any plage or pore, so that the propagation of waves in the chromosphere was less affected by canopy fields.

Active regions with a strong magnetic field show a small contribution of acoustic waves, where the acoustic-flux deposit balances only 10–30% of the radiative losses in the chromosphere between the heights of 1100 and 1800 km (IRIS data sets). The deposited acoustic-energy flux is small and decreases with increasing radiative losses. We may speculate about a reduction of the incoming acoustic flux by the presence of magnetic shadows and a different character of waves in magnetic regions, which do not dissipate so efficiently like the supersonic

shocks. Definitely, the active-region chromosphere is heated by mechanisms different from the magnetoacoustic waves. This finding is consistent with the negligible contribution of magnetoacoustic waves to the heating of the upper chromosphere (1600–1900 km) in active regions (VTT data sets).

We have also shown that in the upper chromosphere, the incoming and deposited acoustic fluxes are very small compared to the radiative losses. In quiet-Sun region, the acoustic-flux deposit contributes only by about 20 % to the radiative losses between the heights 1400 km and 1800 km (BBSO data set) while in weak active regions (VTT data sets), its contribution is practically equal to zero in the height range 1600–1900 km.

This finding may be explained by the fact that the acoustic energy flux at a given height is proportional to the density of gas ρ, power density of Doppler velocities P_v, and the group velocity $v_{\rm gr}$. Of these three quantities, the change of ρ with height is the most important one. Densities in the middle chromosphere are by an order of magnitude higher than those in the upper chromosphere, while $P_v \sim \sigma_v^2$ is approximately of the same order (see Table 2 of Abbasvand et al. (2020b)) and $v_{\rm gr}$ may change by a factor of 3 at maximum. Thus, it is mainly the density that determines the amounts of the incoming and deposited acoustic fluxes, which are considerable in the middle chromosphere but negligible in the upper layers.

The comparison of our results with the extensive literature on chromospheric heating by waves is not straightforward. Different methods with different assumptions were used to find the wave energy flux, giving different results. For example, Carlsson et al. (2007) applied numerical simulations to match observed broadband intensity fluctuations and concluded that the waves do not have enough energy to heat the quiet chromosphere. Bello González et al. (2009) and also our work utilized power spectra of Doppler velocity oscillations and found that the energy deposited by the waves is sufficient. In most of previous cases, the acoustic energy flux was determined in layers below the chromosphere. Our observations allow to calculate the acoustic energy deposited in the middle and upper chromosphere between $z \simeq 900$ and 2000 km and compare it to radiative losses from this range of heights. We cannot include lower layers, but an important part of energy released by radiation comes also from the lower chromosphere. The most reliable comparison should cover all heights in the chromosphere, using 3D radiative transfer and time-dependent model atmospheres.

We would like to emphasize that our results are not inconsistent with the previous studies, where many (e.g., Fossum and Carlsson 2005; Beck et al. 2009, or see a thorough discussion in Section 4.1 of Jess et al. 2015) showed that the (magneto)acoustic waves are not sufficient to explain the heating of the chromosphere. In the present work we only studied two separate layers of the chromosphere available to us in our observations. We have no information about the relations between the deposited acoustic flux and radiative losses in the lower chromosphere. Thus, we do not attempt to draw any conclusions regarding the energy budget of the chromosphere as a whole. We point out that for some layers the heating by (magneto)acoustic waves may be sufficient, whereas in other layers it is insufficient. This fact itself draws a need for an additional source of energy. It is interesting to note that a similar conclusion was drawn by Fawzy et al. (2002) in the case of chromospheres of six late-type main-sequence stars, for which high-quality spectroscopic observations were available.

Although our stationary approach based on time-averaged acoustic fluxes and 1D hydrostatic semi-empirical models might not be fully realistic, it nevertheless opens up a possibility of a general estimate of the role of (magneto)acoustic waves in chromospheric heating by statistical comparison of the deposited acoustic fluxes to the radiative losses. Its results, namely (i) the ability of the quiet-region middle chromosphere to absorb sufficient acoustic-energy

flux to maintain the temperature derived from semi-empirical models and (ii) the substantial reduction of incoming and deposited acoustic fluxes in magnetized active regions, may provide some hints to more realistic studies that use dynamic time-dependent models.

References

Abbasvand, V., Sobotka, M., Heinzel, P., Švanda, M., Jurčák, J., del Moro, D., and Berrilli, F. (2020a). Chromospheric Heating by Acoustic Waves Compared to Radiative Cooling. II. Revised Grid of Models. *ApJ*, 890(1):22.

Abbasvand, V., Sobotka, M., Švanda, M., Heinzel, P., García-Rivas, M., Denker, C., Balthasar, H., Verma, M., Kontogiannis, I., Koza, J., Korda, D., and Kuckein, C. (2020b). Observational study of chromospheric heating by acoustic waves. *A&A*, 642:A52.

Abbasvand, V., Sobotka, M., Švanda, M., Heinzel, P., Liu, W., and Mravcová, L. (2021). IRIS observations of chromospheric heating by acoustic waves in solar quiet and active regions. *A&A*, 648:A28.

Beck, C., Khomenko, E., Rezaei, R., and Collados, M. (2009). The energy of waves in the photosphere and lower chromosphere. I. Velocity statistics. *A&A*, 507(1):453–467.

Bel, N. and Leroy, B. (1977). Analytical Study of Magnetoacoustic Gravity Waves. *A&A*, 55:239.

Bello González, N., Flores Soriano, M., Kneer, F., and Okunev, O. (2009). Acoustic waves in the solar atmosphere at high spatial resolution. *A&A*, 508(2):941–950.

Bello González, N., Flores Soriano, M., Kneer, F., Okunev, O., and Shchukina, N. (2010). Acoustic waves in the solar atmosphere at high spatial resolution. II. Measurement in the Fe I 5434 Å line. *A&A*, 522:A31.

Cally, P. S. (2006). Dispersion relations, rays and ray splitting in magnetohelioseismology. *Phil. Trans. Roy. Soc. London Ser. A*, 364(1839):333–349.

Carlsson, M., Hansteen, V. H., de Pontieu, B., McIntosh, S., Tarbell, T. D., Shine, D., Tsuneta, S., Katsukawa, Y., Ichimoto, K., Suematsu, Y., Shimizu, T., and Nagata, S. (2007). Can High Frequency Acoustic Waves Heat the Quiet Sun Chromosphere? *PASJ*, 59:S663.

Carlsson, M. and Leenaarts, J. (2012). Approximations for radiative cooling and heating in the solar chromosphere. *A&A*, 539:A39.

Carlsson, M. and Stein, R. F. (1992). Non-LTE Radiating Acoustic Shocks and CA II K2V Bright Points. *ApJ*, 397:L59.

Cuntz, M., Rammacher, W., and Musielak, Z. E. (2007). Acoustic Heating of the Solar Chromosphere: Present Indeed and Locally Dominant. *ApJ*, 657(1):L57–L60.

Fawzy, D., Ulmschneider, P., Stępień, K., Musielak, Z. E., and Rammacher, W. (2002). Acoustic and magnetic wave heating in stars . II. On the range of chromospheric activity. *A&A*, 386:983–993.

Fossum, A. and Carlsson, M. (2005). High-frequency acoustic waves are not sufficient to heat the solar chromosphere. *Nature*, 435(7044):919–921.

Garcia, A., Klvaňa, M., and Sobotka, M. (2010). Measurements of chromospheric velocity fields by means of the Coimbra University spectroheliograph. *Central European Astrophysical Bulletin*, 34:47–56.

Ghosh, A., Klimchuk, J. A., and Tripathi, D. (2019). On Doppler Shift and Its Center-to-limb Variation in Active Regions in the Transition Region. *ApJ*, 886(1):46.

Grant, S. D. T., Jess, D. B., Zaqarashvili, T. V., Beck, C., Socas-Navarro, H., Aschwanden, M. J., Keys, P. H., Christian, D. J., Houston, S. J., and Hewitt, R. L. (2018). Alfvén wave dissipation in the solar chromosphere. *Nature Physics*, 14(5):480–483.

Gurtovenko, E., Ratnikova, V., and de Jager, C. (1974). On the Average Optical Depth of Formation of Weak Fraunhofer Lines. *Sol. Phys.*, 37(1):43–52.

Jefferies, S. M., McIntosh, S. W., Armstrong, J. D., Bogdan, T. J., Cacciani, A. r., and Fleck, B. (2006). Magnetoacoustic Portals and the Basal Heating of the Solar Chromosphere. *ApJ*, 648(2):L151–L155.

Jess, D. B., Morton, R. J., Verth, G., Fedun, V., Grant, S. D. T., and Giagkiozis, I. (2015). Multiwavelength Studies of MHD Waves in the Solar Chromosphere. An Overview of Recent Results. *Space Sci. Rev.*, 190(1-4):103–161.

Judge, P. G., Tarbell, T. D., and Wilhelm, K. (2001). A Study of Chromospheric Oscillations Using the SOHO and TRACE Spacecraft. *ApJ*, 554(1):424–444.

Kalkofen, W. (2007). Is the Solar Chromosphere Heated by Acoustic Waves? *ApJ*, 671(2):2154–2158.

Kanoh, R., Shimizu, T., and Imada, S. (2016). Hinode and IRIS Observations of the Magnetohydrodynamic Waves Propagating from the Photosphere to the Chromosphere in a Sunspot. *ApJ*, 831(1):24.

Kayshap, P., Murawski, K., Srivastava, A. K., Musielak, Z. E., and Dwivedi, B. N. (2018). Vertical propagation of acoustic waves in the solar internetworkas observed by IRIS. *MNRAS*, 479(4):5512–5521.

Kontogiannis, I., Tsiropoula, G., and Tziotziou, K. (2010). Power halo and magnetic shadow in a solar quiet region observed in the Hα line. *A&A*, 510:A41.

Leenaarts, J. (2020). Radiation hydrodynamics in simulations of the solar atmosphere. *Living Reviews in Solar Physics*, 17(1):3.

Rieutord, M., Roudier, T., Rincon, F., Malherbe, J. M., Meunier, N., Berger, T., and Frank, Z. (2010). On the power spectrum of solar surface flows. *A&A*, 512:A4.

Rybicki, G. B. and Hummer, D. G. (1991). An accelerated lambda iteration method for multilevel radiative transfer. *A&A*, 245:171–181.

Rybicki, G. B. and Hummer, D. G. (1992). An accelerated lambda iteration method for multilevel radiative transfer. II. Overlapping transitions with full continuum. *A&A*, 262:209–215.

Sobotka, M., Heinzel, P., Švanda, M., Jurčák, J., del Moro, D., and Berrilli, F. (2016). Chromospheric Heating by Acoustic Waves Compared to Radiative Cooling. *ApJ*, 826(1):49.

Testa, P., De Pontieu, B., Allred, J., Carlsson, M., Reale, F., Daw, A., Hansteen, V., Martinez-Sykora, J., Liu, W., DeLuca, E. E., Golub, L., McKillop, S., Reeves, K., Saar, S., Tian, H., Lemen, J., Title, A., Boerner, P., Hurlburt, N., Tarbell, T. D., Wuelser, J. P., Kleint, L., Kankelborg, C., and Jaeggli, S. (2014). Evidence of nonthermal particles in coronal loops heated impulsively by nanoflares. *Science*, 346(6207):1255724.

Ulmschneider, P. and Musielak, Z. (2003). Mechanisms of Chromospheric and Coronal Heating (Invited review). In Pevtsov, A. A. and Uitenbroek, H., editors, *Current Theoretical Models and Future High Resolution Solar Observations: Preparing for ATST*, volume 286 of *ASP Conf. Ser.*, page 363.

Vecchio, A., Cauzzi, G., Reardon, K. P., Janssen, K., and Rimmele, T. (2007). Solar atmospheric oscillations and the chromospheric magnetic topology. *A&A*, 461(1):L1–L4.

Vernazza, J. E., Avrett, E. H., and Loeser, R. (1981). Structure of the solar chromosphere. III. Models of the EUV brightness components of the quiet sun. *ApJS*, 45:635–725.

Wedemeyer-Böhm, S., Steiner, O., Bruls, J., and Rammacher, W. (2007). What is Heating the Quiet-Sun Chromosphere? In Heinzel, P., Dorotovič, I., and Rutten, R. J., editors, *The Physics of Chromospheric Plasmas*, volume 368 of *Astronomical Society of the Pacific Conference Series*, page 93.

Withbroe, G. L. and Noyes, R. W. (1977). Mass and energy flow in the solar chromosphere and corona. *ARA&A*, 15:363–387.

Zaqarashvili, T. V. and Erdélyi, R. (2009). Oscillations and Waves in Solar Spicules. *Space Sci. Rev.*, 149(1-4):355–388.

International experience

During my doctoral studies, I participated in several research stays, observations, and meetings, namely:

- VTT and GREGOR Observations at the Teide Observatory, Tenerife, December 2018 and June 2019. Observations: waves measured in chromospheric lines in quiet Sun and plages.
- Meeting between 23-25 April 2018 at the Leibniz Institute for Astrophysics Potsdam (AIP), Potsdam, Germany, regarding problems of line inversion methods.
- Meeting with the AIP Solar physics group between 9-11 April 2019 at the Astronomical Institute of the Czech Academy of Sciences (ASU), Ondřejov, Czech Republic. Presentation: "Grid of Semi-empirical Models to Study the Chromospheric Heating".
- Seminar at the Department of Solar Physics, ASU, Ondřejov, May 30, 2019, title of presentation: "A Grid of Semi-empirical Models Used to Study the Chromospheric Heating"
- Staying between 15-29 July 2019 at Leibniz Institute for Astrophysics Potsdam (AIP), Potsdam, Germany, reducing the observed data.
- Participation in the SOLARNET-FoMICS school on "Solar spectropolarimetry: From virtual to real observations", Sept. 9-14, 2019, Universitá della Svizzera italiana (USI) and Istituto Ricerche Solari Locarno (IRSOL), Lugano, Switzerland.
- Staying between 25 November-2 December 2019 at Leibniz Institute for Astrophysics Potsdam (AIP), Potsdam, Germany, analysing Hα and Hβ Doppler velocity power spectra.
- 25th Solar Physics Meeting, Hurbanovo, Slovakia, October 20-22, 2020, online. Title of presentation: "Chromospheric heating by acoustic waves II – Middle and upper chromosphere"
- Online Astronomical Institute Seminar, ASU, Ondřejov, December 14, 2020, title of presentation: "Chromospheric heating by acoustic waves compared by radiative cooling"